

# 1 Quantifying Effects of Earth Orbital Parameters and 2 Greenhouse Gases on Mid-Holocene Climate

3 Yibo Kang and Haijun Yang\*

4 Department of Atmospheric and Oceanic Sciences and Institute of Atmospheric Science and CMA-FDU Joint  
5 Laboratory of Marine Meteorology, Fudan University, Shanghai, 200438, China.  
6 Shanghai Scientific Frontier Base for Ocean-Atmosphere Interaction Studies, Fudan University, Shanghai 200438,  
7 China.

8 *Correspondence to:* Haijun Yang ([yanghj@fudan.edu.cn](mailto:yanghj@fudan.edu.cn))

9 **Abstract.** The mid-Holocene (MH) is the most recent typical climate period, and a subject of great interest in global  
10 paleocultural research. Following the latest Paleoclimate Modelling Intercomparison Project phase 4 (PMIP4) protocol  
11 and using a fully coupled climate model, we simulated the climate during both the MH and the pre-industrial (PI)  
12 periods, and quantified the effects of Earth orbital parameters (ORB) and greenhouse gases (GHG) on climate  
13 differences, focusing on the simulated differences in the Atlantic meridional overturning circulation (AMOC) between  
14 these two periods. Compared to the PI simulation, the ORB effect in the MH simulation led to seasonal enhancement  
15 of temperature, consistent with previous findings. In the MH simulation, the ORB effect led to a markedly warmer  
16 climate in the mid-to-high latitudes and increased precipitation in the Northern Hemisphere, which were partially  
17 offset by the cooling effect of the lower GHG. The AMOC in the MH simulation was about 4% stronger than that in  
18 the PI simulation. The ORB effect led to 6% enhancement of the AMOC in the MH simulation, which was, however,  
19 partly neutralized by the GHG effect. Transient simulation from the MH to the PI further demonstrated opposite  
20 effects of ORB and GHG on the evolution of the AMOC during the past 6000 years. The simulated stronger AMOC in  
21 the MH was mainly due to the thinner sea ice in the polar oceans caused by the ORB effect, which reduced the  
22 freshwater flux export to the subpolar Atlantic and resulted in a more saline North Atlantic. This study may help us  
23 quantitatively understand the roles of different external forcing factors in Earth's climate evolution since the MH.  
24 **Keywords:** Mid-Holocene, Earth orbital parameters, Greenhouse gases, Atlantic Meridional Overturning Circulation

25

26

## 27 **1. Introduction**

28 The mid-Holocene (MH; 6000 years before the present) is a period of profound cultural transition worldwide,  
29 particularly in the arid-semi-arid belt of  $\sim 30^\circ\text{N}$  (Sandweiss et al., 1999; Moss et al., 2007; Roberts et al., 2011;  
30 Warden et al., 2017). The MH climate, which belongs to the Holocene climatic optimum (Rossignol-Strick, 1999;  
31 Chen et al., 2003; Zhang et al., 2020), differs notably from that of the subsequent period. Many studies have shown  
32 that the development of human civilization during this period was influenced by the climate, which was closely related  
33 to external factors such as the Earth's orbital parameters (ORB), greenhouse gases (GHG), and solar constants (Jin,  
34 2002; Wanner et al., 2008; Warden et al., 2017). Therefore, it is of great interest to study the MH climate, for a better  
35 understanding of the influence of external forcing factors on human civilization.

36 As the key benchmark period of the Paleoclimate Modelling Intercomparison Project (PMIP) program  
37 (Joussaume and Taylor, 1995; Kageyama et al., 2018), the MH experiment was designed to examine climate response  
38 to a change in the seasonal and latitudinal distribution of incoming solar radiation caused by known changes in Earth  
39 orbital forcing. As the program evolved, the GHG concentrations used in the MH experiments are closer to the true  
40 values (Monnin et al., 2001, 2004). However, most studies focused on the general climate differences between the MH  
41 and pre-industrial (PI) periods; the individual effects of the ORB and GHG on the climate itself are not isolated. Some  
42 studies examined the role of GHG by comparing different PMIP programs. Otto-Bliesner et al. (2017) found that the  
43 change in the experimental protocol between PMIP phase 4 and PMIP phase 3 (PMIP4 and PMIP3 hereafter,  
44 respectively), with a reduction in  $\text{CO}_2$  concentration from 280 to 264.4 ppm, would reduce GHG forcing by about 0.3  
45  $\text{W/m}^2$ . This change can produce an estimated global mean cooling in surface air temperature (SAT) of about  $0.28^\circ\text{C}$   
46 based on the climate sensitivity of difference models in PMIP4 (Brierley et al., 2020). The GHG contribution to  
47 temperature change is small, but not negligible. Quantifying the effects of ORB and GHG on the difference between  
48 the MH and PI has important implications for a deeper understanding of the roles played by external forcing factors in  
49 the past climate.

50 The Atlantic meridional overturning circulation (AMOC) is considered an important heat transmitter of the  
51 Earth's climate system, which affects global climate on various timescales (Rahmstorf, 2006). Paleoclimate studies  
52 showed that the weakening or stopping of the AMOC can result in substantial cooling across the Northern Hemisphere  
53 (NH) (Brown and Galbraith, 2016; Yan and Liu, 2019). In recent years, predictions concerning future behavior of the  
54 AMOC by the Intergovernmental Panel on Climate Change (IPCC) are accompanied by notable uncertainties,  
55 particularly due to the substantial variability in anticipated AMOC changes under different emission scenarios (Fox-  
56 Kemper et al., 2021). Therefore, simulating past AMOC changes and exploring the effects of different forcing factors

57 on its behavior will help us understand the nature of abrupt climate change in the past and mitigate uncertainties in  
58 future climate projections. In the previous MH simulations of the PMIP, the AMOC was generally stronger than that  
59 of the PI (Găinușă-Bogdan et al., 2020); this change in the AMOC is related to sea ice feedback, and the simulation  
60 results may be slightly different due to model or resolution differences (Shi and Lohmann, 2016; Shi et al., 2022).  
61 Recent studies suggested that the difference of the AMOC between the MH and PI periods in PMIP4 ensemble  
62 simulation is not significant (Brierley et al., 2020). By comparing the strength of the AMOC during the interglacial  
63 period, it was found that the variation range of the AMOC in the MH is within the internal variability range of all  
64 models; and the ORB does not seem to have played a role (Jiang et al., 2023a). By examining multi-model transient  
65 simulations that all include two or more external forcing factors, Jiang et al. (2023b) reported that the AMOC did not  
66 change much from the MH to the PI, which is consistent with some proxy reconstructions.

67 In this paper, we further study the mechanism of weak difference of the AMOC between the MH and PI periods.  
68 The effects of different external forcings on the AMOC are quantified through several sensitivity experiments.  
69 Multiple transient experiments are also performed to verify the roles of different forcing factors in long-term climate  
70 evolution. This paper is structured as follows. An introduction to the fully coupled climate model is given in section 2,  
71 along with experimental design. In section 3, we present the effects of ORB and GHG on the MH climate, and their  
72 effects on the Hadley cell and AMOC. The changes of North Atlantic Ocean buoyancy between the MH and PI  
73 periods in both equilibrium and transient experiments are described in section 4. Summary and discussion are given in  
74 section 5.

75

## 76 **2. Model and experiments**

77 The coupled model used in this study is the National Centre for Atmospheric Research's Community Earth  
78 System Model version 1.0 (CESM1.0). It includes atmospheric, oceanic, sea-ice, and land model components. The  
79 atmospheric model consists of 26 vertical levels and T31 horizontal resolution (roughly  $3.75^\circ \times 3.75^\circ$ ). The land model  
80 shares the same horizontal resolution as the atmospheric model. The ocean model has 60 vertical levels, and employs  
81 gx3v7 horizontal resolution. In the zonal direction, the grid has a uniform  $3.6^\circ$  spacing. In the meridional direction, the  
82 grid is nonuniformly spaced: it is  $0.6^\circ$  near the equator, gradually increases to the maximum  $3.4^\circ$  at  $35^\circ\text{N}/^\circ\text{S}$ , and then  
83 decreases poleward. The sea-ice model has the same horizontal resolution as the ocean model. More details on these  
84 model components can be found in a number of studies (Smith and Gent, 2010; Hunke and Lipscomb, 2010; Lawrence  
85 et al., 2012; Park et al., 2014).

86 To quantify the effects of ORB and GHG on climate differences between the MH and PI periods, we designed  
87 three sensitivity experiments following the PMIP4 protocol (Table 1). Exp MH uses the ORB and GHG in the MH  
88 period. Exp MH\_ORB uses the ORB in the MH period and the GHG in the PI period. Exp PI uses the ORB and GHG  
89 in the PI period. Note that our simulations do not intend to compare climate states between PMIP3 and PMIP4; we  
90 want to isolate the individual effects of ORB and GHG within the framework of the PMIP4. There are differences  
91 between PMIP3 and PMIP4 in solar constant and GHG concentration. By tightly controlling the external forcings in  
92 the different experiments, our simulations effectively isolate the external forcing component compared to PMIP3, not  
93 just the ORB. The solar constant in the three experiments is set to 1360.75 W/m<sup>2</sup>. The specific values of the ORB are  
94 listed in Table 1 (Berger and Loutre, 1991); and the GHG data comes from the ice-core records of the Antarctica and  
95 Greenland (Otto-Bliesner et al., 2017). The vernal equinox is set to noon on 21 March. Exps MH and MH\_ORB start  
96 from the PI condition, and each of the three experiments is integrated for 2000 years and reaches the equilibrium by  
97 then (Fig. 5a). The effect of ORB is obtained by subtracting Exp PI from Exp MH\_ORB, and the effect of GHG is  
98 obtained by subtracting Exp MH\_ORB from Exp MH. The combined effect of ORB and GHG is obtained by  
99 subtracting Exp PI from Exp MH. In this paper, we use the monthly mean data of the last 500 years of each model  
100 simulation for analysis (Fig. 5a).

101 To enhance the rigor of our study and confirm the effects of ORB and GHG on the climate evolution from the  
102 MH to the PI, we conducted three additional transient experiments (Table 2). Each transient experiment starts at the  
103 MH and concludes at the PI, spanning a total of 5900 model years. Exp ORB represents the transient experiment for  
104 ORB; Exp GHG, the transient experiment for GHG; and Exp Full, the experiment where ORB, GHG, and total solar  
105 irradiance are applied concurrently. The ORB data in the transient experiments is from Berger and Loutre (1991), the  
106 GHG data is interpolated from GHG data reconstructed from Antarctic ice cores, and the total solar irradiance data is  
107 from the PMIP4 SATIRE-M solar forcing data (Otto-Bliesner et al., 2017). We use model years 1–500 to represent the  
108 MH climate (Stage 1) and model years 5401–5900 to represent the PI climate (Stage 2), and then compare the  
109 difference between Stage 1 and Stage 2 to the results of the equilibrium experiments (Fig. 5b). The settings for forcing  
110 information in the transient experiments are listed in Table 2.

111  
112 **Table 1. Forcings and boundary conditions in equilibrium experiments. More details can be found in Otto-Bliesner et al.**  
113 **(2017).**

	Exp MH	Exp PI	Exp MH_ORB
Orbital parameters			Same as Exp MH
Eccentricity	0.018682	0.016764	0.018682

Obliquity (degrees)	24.105	23.459	24.105
Perihelion – 180	0.87	100.33	0.87
Greenhouse gases			Same as Exp PI
CO <sub>2</sub> (ppm)	264.4	284.3	284.3
CH <sub>4</sub> (ppb)	597	808.2	808.2
N <sub>2</sub> O (ppb)	262	273.0	273.0

114

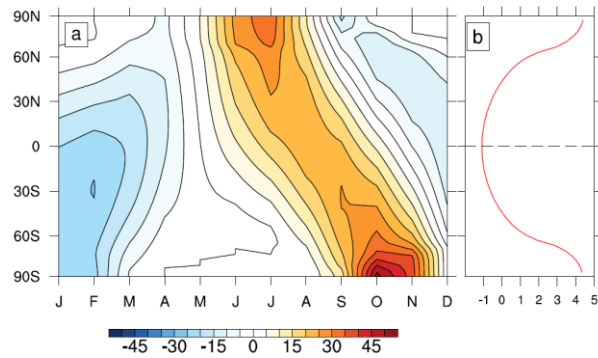
115

**Table 2. Forcing and boundary conditions in transient experiments.**

	Exp ORB	Exp GHG	Exp Full
Orbital parameters	Berger and Loutre (1991)	Same as Exp MH Flückiger et al. (2002)	Same as Exp ORB
Greenhouse gases	Same as Exp MH	Monnin et al. (2004) Spahni et al. (2005)	Same as Exp GHG
Total solar irradiance	Same as Exp MH	Same as Exp MH	Otto-Bliesner et al. (2017)

116

117 Orbital parameters include eccentricity, precession, and obliquity. In the past six millennia, both eccentricity and  
118 obliquity did not change much. The main change came from precession, which is influenced by eccentricity and the  
119 longitude of perihelion. As a result, perihelion is close to the NH autumn equinox in the MH period and close to the  
120 NH winter solstice in the PI period. Therefore, with respect to Exp PI, the solar energy received at the top of the  
121 atmosphere (TOA) in Exp MH changed seasonally and latitudinally, as shown in Fig. 1a. Compared to Exp PI, Exp  
122 MH had higher NH summer radiation and lower winter radiation, and the difference during June–August (JJA)  
123 reached 30 W/m<sup>2</sup> in the high latitudes. Smaller precession led to more radiation received in the NH summer in the MH  
124 period. Figure 1b shows the meridional variation of annual mean shortwave radiation at the TOA, which is greater  
125 than 4 W/m<sup>2</sup> poleward of 45°N(S), but negative and smaller than 1 W/m<sup>2</sup> between 45°S and 45°N. This situation is  
126 associated with the larger obliquity in the MH (Otto-Bliesner et al., 2006; Williams et al., 2020). In addition, the  
127 difference of GHG between the MH and PI periods can lead to an effective radiative forcing of 0.3 W/m<sup>2</sup> (Otto-  
128 Bliesner et al., 2017).



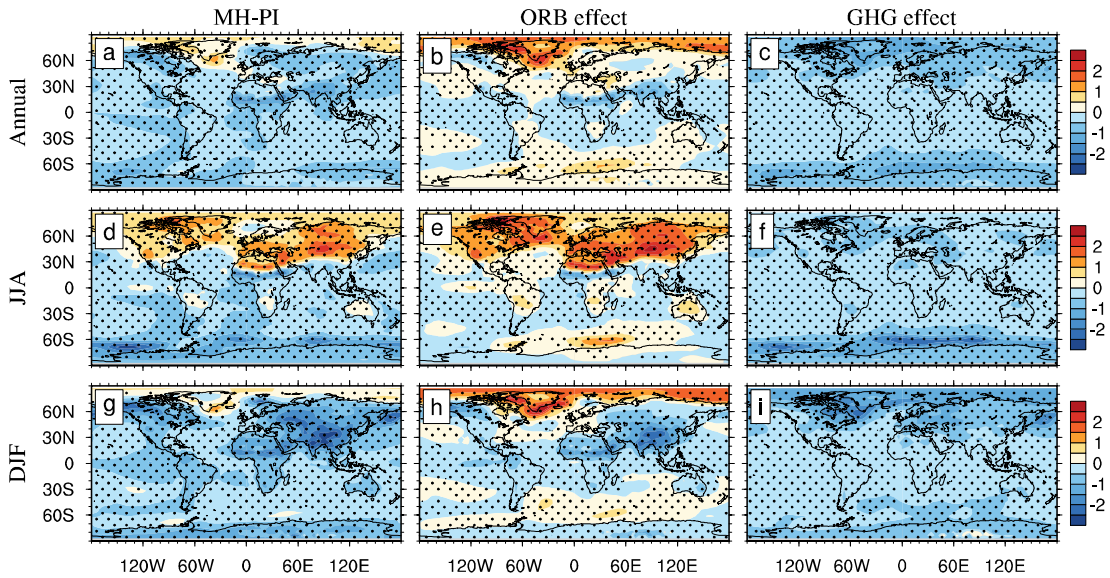
129

130 **Figure 1 (a) Latitude-month distribution of solar radiation change at the TOA in Exp MH, and (b) annual mean solar**  
 131 **radiation change, with respect to Exp PI. Units: W/m<sup>2</sup>.**

132 **3. Results**

133 **3.1 Surface air temperature and precipitation**

134 Compared to Exp PI, Exp MH has warmer annual mean temperatures in the NH high latitudes and cooler  
 135 temperatures in the rest of the globe (Fig. 2a), while Exp MH\_ORB has a warmer surface at mid–high latitudes in both  
 136 the NH and SH, with a greater range and magnitude than Exp MH (Fig. 2b). Figure 2b shows direct response to the  
 137 meridional change of annual mean solar radiation. The lower GHG in the MH contributed to a lower global surface  
 138 temperature, which is clear in the mid–high latitudes (Fig. 2c). In the NH summer (June–August, or JJA), Exp MH  
 139 shows a general warming of more than 1°C north of 30°N, which is more significant in Greenland and Euro-Asian  
 140 continent, and a cooling belt in northern India and central Africa (Fig. 2d), which is associated with increased rainfall  
 141 due to the enhanced monsoon (Fig. 2d). The magnitude and extent of warming due to the ORB effect are apparently  
 142 greater, with warming of up to 3°C in central Asia (Fig. 2e). The GHG cooling is more pronounced over the Southern  
 143 Ocean (Fig. 2f). In the NH winter (December–February, or DJF), only the NH polar latitudes remain the warming.  
 144 There is strong cooling (up to 3°C) in the African and Euro-Asian continents (Fig. 2g). The patterns under the ORB  
 145 and GHG forcing are similar to their annual mean situations, except for the enhanced cooling in South Asia and  
 146 central Africa (Fig. 2h) and over the subpolar Atlantic (Fig. 2i). Most figures show polar amplification, which may be  
 147 related to the change of sea ice (Otto-Bliesner et al., 2017; Williams et al., 2020).

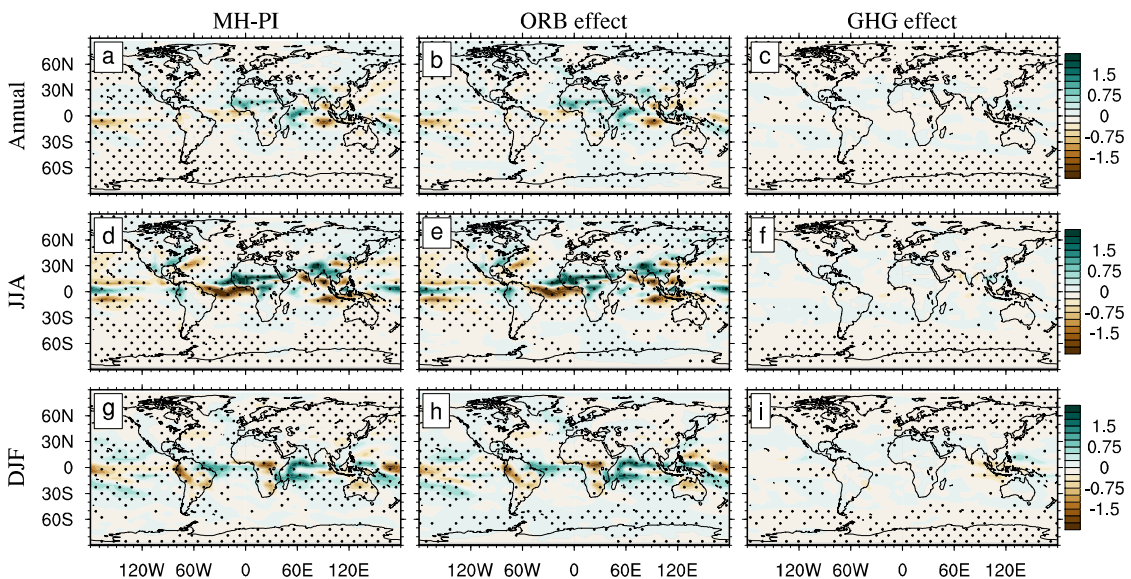


148

149 **Figure 2** (Left column) Changes in SAT in Exp MH, with respect to Exp PI, and the contributions from (central column)  
 150 the ORB effect and (right column) the GHG effect. (a)–(c) are for annual mean; (d)–(f), for NH JJA; and (g)–(i), for NH  
 151 DJF. Stippling shows significance over the 90% level calculated by Student *t*-test. Units: °C.

152

153 Differences in precipitation between the MH and PI simulations are shown in Fig. 3. Consistent with the  
 154 latitudinal and seasonal differences of insolation (Fig. 1), the largest difference in precipitation between the two  
 155 periods also occurs in the NH summer, with significantly more precipitation in northern India and equatorial African  
 156 monsoon region, and drier in the equatorial Atlantic and Pacific in Exp MH (Fig. 3d). The difference between Exps  
 157 MH and PI is mainly in the global tropics, and is contributed predominantly by the ORB effect (Figs. 3e, h), as the  
 158 GHG effect is very weak (Figs. 3f, i).



159

160 **Figure 3** Same as Fig. 2, but for precipitation change. Units: mm/day.

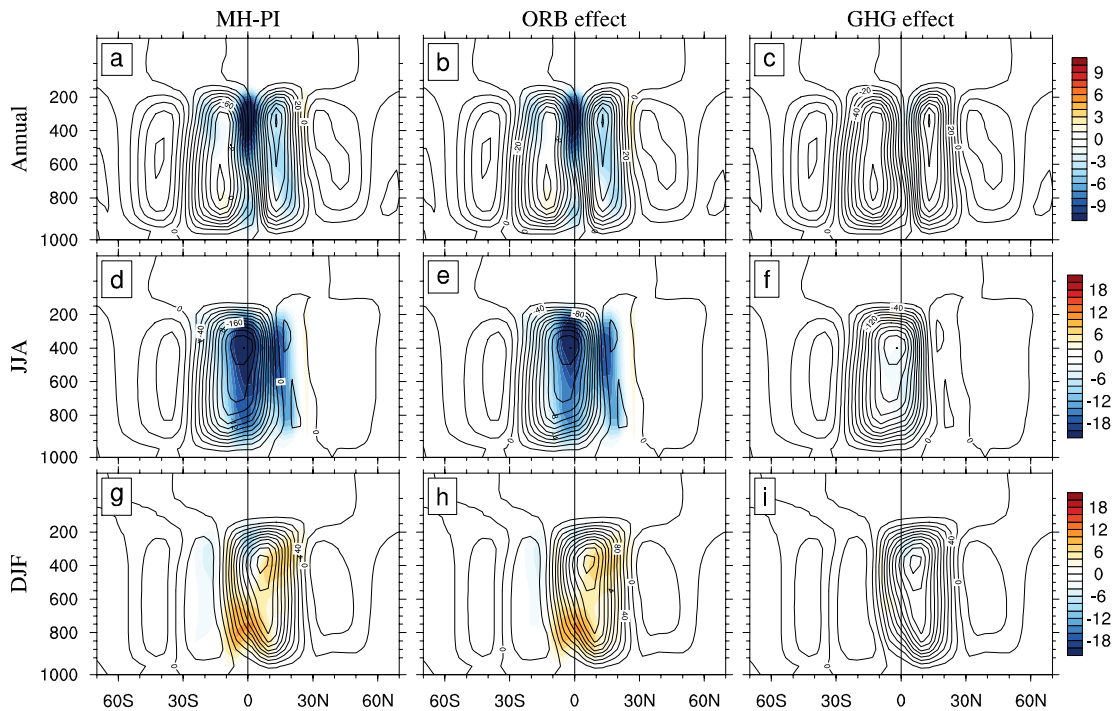
161

162 Although the numerical values may be slightly different due to different models or resolutions, in general the  
163 annual and seasonal climatology differences of temperature and precipitation between Exps MH and PI are in good  
164 agreement according to recent studies (Williams et al., 2020; Zhang et al., 2021b). The ORB effect dominates the  
165 changes in global surface temperature and precipitation. Thus, Exp MH has a warmer climate than Exp PI, particularly  
166 in NH high latitudes.

167

### 168 3.2 Meridional atmospheric circulation

169 The meridional atmospheric circulation, namely, the Hadley cell, in Exp MH is about 10% weaker than that in  
170 Exp PI (Fig. 4a), consistent with the weaker meridional atmospheric temperature gradient in Exp MH than in Exp PI.  
171 The weaker Hadley cell in Exp MH is mainly due to the ORB effect (Figs. 4b, e, h). The GHG effect can be neglected  
172 (Figs. 4c, f, i). The Hadley cell is weaker due to the strong warming of the high-latitude temperatures in the NH  
173 summer (Fig. 4d). The strengthening of the Hadley cell in the NH winter (Fig. 4g) corresponds to an increasing  
174 temperature gradient between the tropics and mid latitudes (Fig. 2g). The weaker Hadley cell also leads to a weaker  
175 meridional atmospheric heat transport from low to high latitudes, which will be discussed in section 3.4.



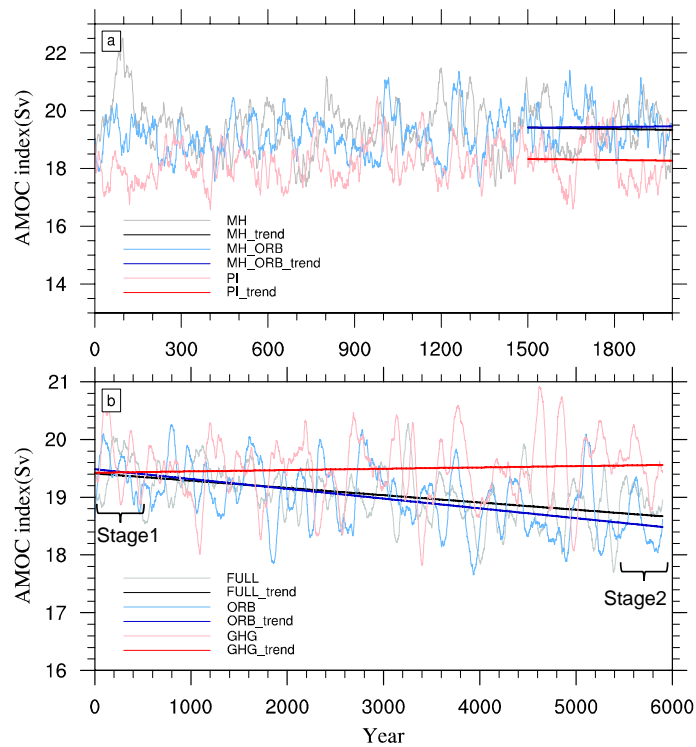
176

177 **Figure 4** Same as Fig. 2, but for the mean Hadley cell in Exp PI (contour) and its changes (shading) in Exp MH. Units:  $10^9$   
178 kg/s.



180 **3.3 Atlantic meridional overturning circulation**

181 The AMOC strength, defined as the maximum streamfunction between 0 and 2000 m and between 20° and 70°N  
 182 in the North Atlantic, are 19.4 and 18.3 Sv in Exps MH and PI, respectively. Figure 5a shows the time series of the  
 183 AMOC of the three equilibrium experiments, all of which reached the equilibrium state. The AMOC in Exp MH\_ORB  
 184 (dark blue line) is 1 Sv stronger than that in Exp PI (dark red line), while the AMOC in Exp MH (dark black line) is  
 185 roughly the same as that in Exp MH\_ORB. Figure 5b shows the evolution of the AMOC in the three transient  
 186 experiments. In Exp ORB, the AMOC strength shows a downward trend (dark blue line). In Exp GHG, the AMOC  
 187 strength exhibits a slight increase with an indistinct trend (dark red line). In Exp Full, the trend of AMOC strength is  
 188 essentially between Exps ORB and GHG, indicating a combined effect of external forcing factors (dark black line).



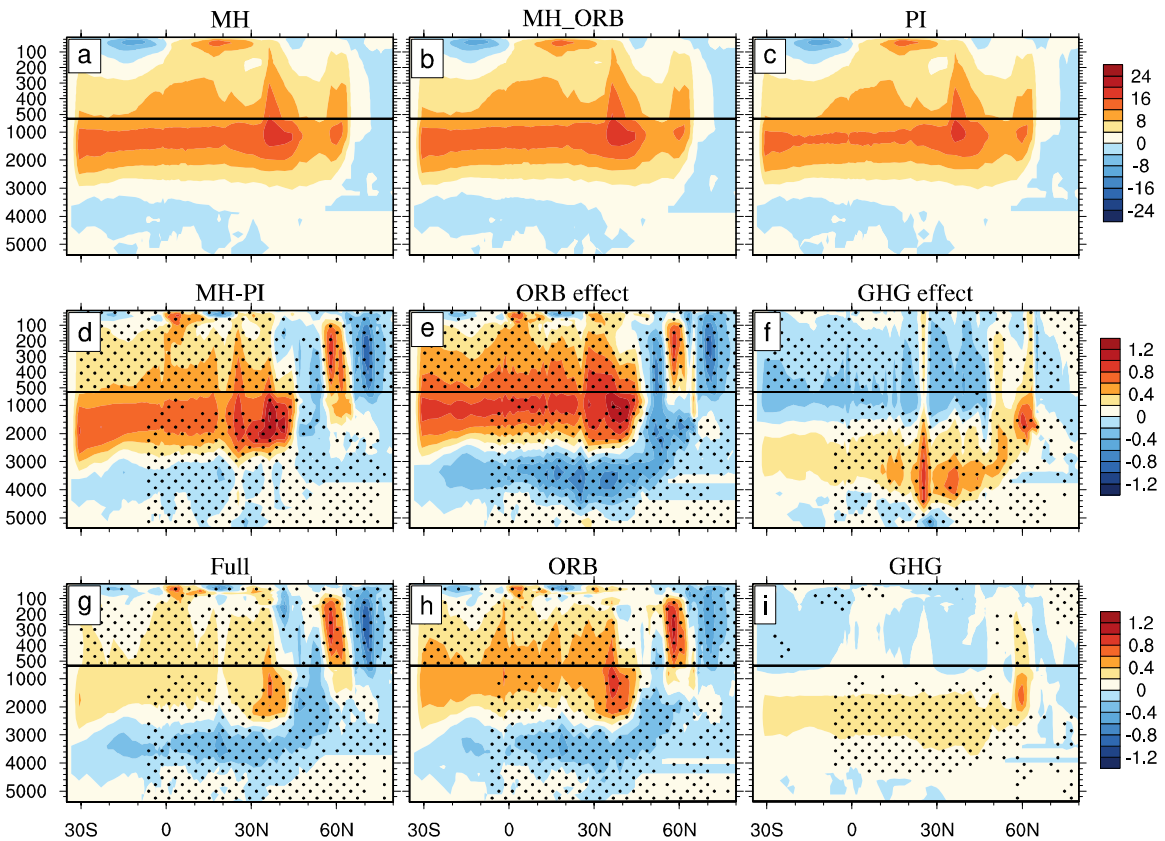
189

190 **Figure 5 (a) Evolutions of the AMOC in Exp MH (gray and black lines), Exp MH\_ORB (blue lines), and Exp PI (red lines).**  
 191 **(b) Evolutions of the AMOC in Exp Full (gray and black lines), Exp ORB (blue lines), and Exp GHG (red lines). The thick**  
 192 **lines indicate the linear trends of the AMOC in different experiments. Units: Sv (1 Sv=10<sup>6</sup> m<sup>3</sup>/s).**

193

194 The patterns of the AMOC are shown in Fig. 6; the depth of the maximum AMOC in all experiments occurs near  
 195 1000 m. The AMOC patterns in Exps MH and PI are similar (Figs. 6a, c), which suggests that the combined effect of  
 196 the ORB and GHG on the AMOC is small (Fig. 6d). This is similar to some recent studies, even though there are

197 slight differences north of 45°N (Brierley et al., 2020; Williams et al., 2020). Individual effects of the ORB and GHG  
 198 are not negligible (Figs. 6e, f). In fact, the ORB effect leads to 6% stronger AMOC in Exp MH than in Exp PI (Fig.  
 199 6e). The deep overturning is significantly enhanced south of 45°N, but slightly weakened north of 45°N. However, at  
 200 the same time the GHG effect leads to a slight decline in AMOC strength in Exp MH, especially above 1500 m south  
 201 of 45°N (Fig. 6f). The ORB and GHG have opposite effects on the AMOC, which make the AMOC in Exp MH  
 202 roughly the same as that in Exp PI. Figure 6g-i further shows the effects of different forcing factors on the AMOC  
 203 patterns in the transient experiments, which are similar to the changes in the equilibrium experiments (Figs. 6d–f),  
 204 although there are differences in intensity. The offset effect between ORB and GHG in the transient experiments is the  
 205 same as that in the equilibrium experiments. Some scholars have suggested that the change of AMOC in Exp MH may  
 206 come from internal variability (Williams et al., 2020), but it is clear from our simulations that changes in response to  
 207 external forcings are the main reason for the variations that occur in Exp MH.



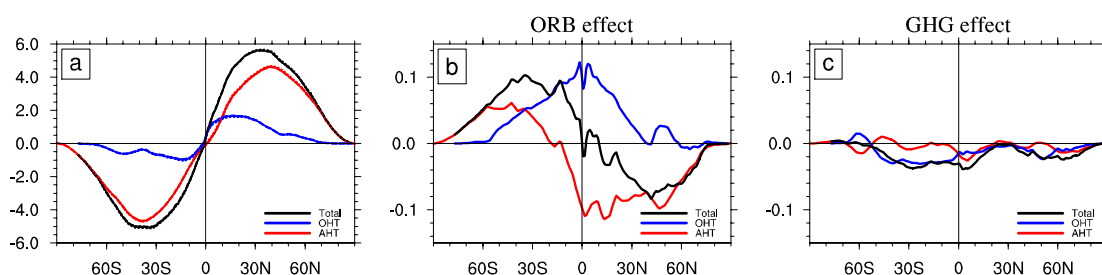
208  
 209 **Figure 6** Patterns of mean AMOC in (a) Exp MH, (b) Exp MH\_ORB, and (c) Exp PI; and (d) AMOC change in Exp MH,  
 210 with respect to Exp PI. (e) and (f) show AMOC changes due to the ORB effect and GHG effect, respectively. g, h, i represent  
 211 the AMOC changes between the two stages (Stage1-Stage2) in Exps Full, ORB, and GHG, respectively. The AMOC index is  
 212 defined as the maximum streamfunction in the range of 0–2000 m of 20°–70°N in the North Atlantic. Stippling shows  
 213 significance over the 90% level calculated by Student t-test. Units: Sv.

214

### 215 3.4 Meridional heat transport

216 Meridional heat transport (MHT) plays an important role in maintaining energy balance of the Earth climate  
217 system. Figure 7a shows the annual MHTs in different experiments, which are nearly identical. The climate  
218 differences between Exps MH and PI hardly change the integrated heat transport in both the atmosphere and ocean.  
219 Consistent with previous studies (Trenberth and Caron, 2001), the annual mean MHT shows an antisymmetric  
220 structure about the equator, with the peak value of about 5.5 PW (1 PW= $10^{15}$ W) at 40°N/S. Compared with ocean  
221 heat transport (OHT), the atmosphere heat transport (AHT) dominates at most latitudes, which is also consistent with  
222 previous studies (Held, 2001; Wunsch, 2005; Czaja and Marshall, 2006).

223 However, the MHT changes caused by the ORB and GHG effects appear to be nonnegligible. The ORB causes  
224 an increase in OHT in the NH, with the maximum change of about 0.10 PW near the equator, roughly 10% of the  
225 mean OHT there. This is due to the enhanced AMOC, and is the main cause of temperature increase in the NH high  
226 latitudes (Fig. 2b). The northward AHT is reduced, with the maximum change of about 0.10 PW. This is due to the  
227 weakened Hadley cell. The AHT change compensates the OHT change very well in the deep tropics, while the former  
228 overcompensates the latter in the NH off-equatorial regions (Fig. 7b). The GHG effect on the MHT is very weak, with  
229 the maximum MHT change of no more than 0.04 PW near 5°N (Fig. 7c), which is just one third of the ORB-induced  
230 MHT change (Fig. 7b).



231  
232 **Figure 7** (a) Annual mean meridional heat transport (MHT). Black, red, and blue lines are for the total MHT, AHT, and  
233 OHT, respectively. Solid, dashed, and dotted lines are for Exps MH, MH\_ORB, and PI, respectively. (b) and (c) show  
234 changes in the total MHT, AHT, and OHT due to ORB and GHG effects, respectively. Units: PW (1 PW =  $10^{15}$  W).

235

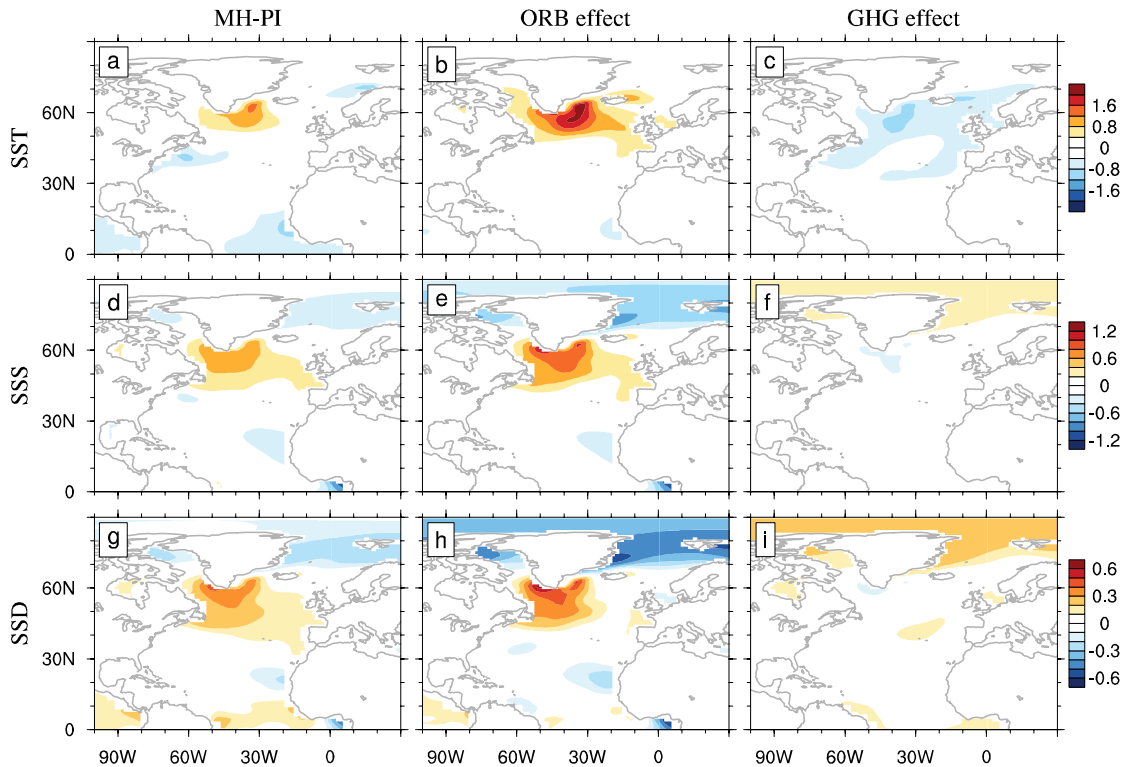
## 236 4. Changes in North Atlantic Ocean

### 237 4.1 Changes in sea-surface temperature, salinity, and density

238 The strength of the AMOC is largely determined by the North Atlantic deep-water formation, which is in turn  
239 determined by upper-ocean density. Figures 8 and 9 show the differences of sea-surface temperature (SST), salinity

240 (SSS), and density (SSD) in the North Atlantic between Exps MH and PI, and the two stages in the transient  
241 experiments, respectively. The SST difference is characterized by a warming up to 1.6°C in the subpolar Atlantic and a  
242 cooling of about 1°C near the Nordic Seas and Gulf Stream extension region (Fig. 8a). The surface ocean warming in  
243 the North Atlantic is due to the ORB effect (Fig. 8b), which causes a strong and extensive warming in the North  
244 Atlantic, with the maximum warming in the subpolar Atlantic. This is in contrast to the warming hole shown by  
245 observations, which are dominated by the cooling of the North Atlantic in the context of global warming. The GHG  
246 effect causes a general cooling in the North Atlantic (Fig. 8c), offsetting partially the ORB-induced warming, leaving  
247 a cooling in the Nordic Seas and Gulf Stream extension (Fig. 8a). The North Atlantic SST change in Exp Full (Fig. 9a)  
248 is consistent with that of Exp MH (Fig. 8a), although the magnitude is slightly smaller. Exp ORB also exhibits  
249 stronger warming than Exp Full (Fig. 9b), consistent with Fig. 8b. Exp GHG shows a slight cooling (Fig. 9c),  
250 consistent with Fig. 8c. Overall, the SST change in the transient experiments is the same as that in the equilibrium  
251 experiments.

252 The patterns of SSS difference between Exps MH and PI are similar to those of SST difference. In general, the  
253 North Atlantic is more saline in Exp MH than in Exp PI (Fig. 8d), mainly due to stronger evaporation over  
254 precipitation in Exp MH than in Exp PI (Fig. 12d), which is in turn due to the warmer SST forced by the ORB effect  
255 (Fig. 8e). The polar oceans are fresher in Exp MH than in Exp PI (Figs. 8d, e), mainly due to more freshwater flux  
256 coming from sea ice in Exp MH (Figs. 12a, b), consistent with the warmer climate in the MH due to the ORB effect.  
257 The SSS difference caused by the GHG effect is roughly opposite to that caused by the ORB effect, but with much  
258 weaker magnitude (Fig. 8f), because the cooling effect of the GHG makes less evaporation in the subtropical–subpolar  
259 Atlantic and more sea ice in the polar oceans (Fig. 12c). Similar to the equilibrium experiments, the SSS changes in  
260 the transient experiments show similar characteristics (Figs. 9d, e, f).

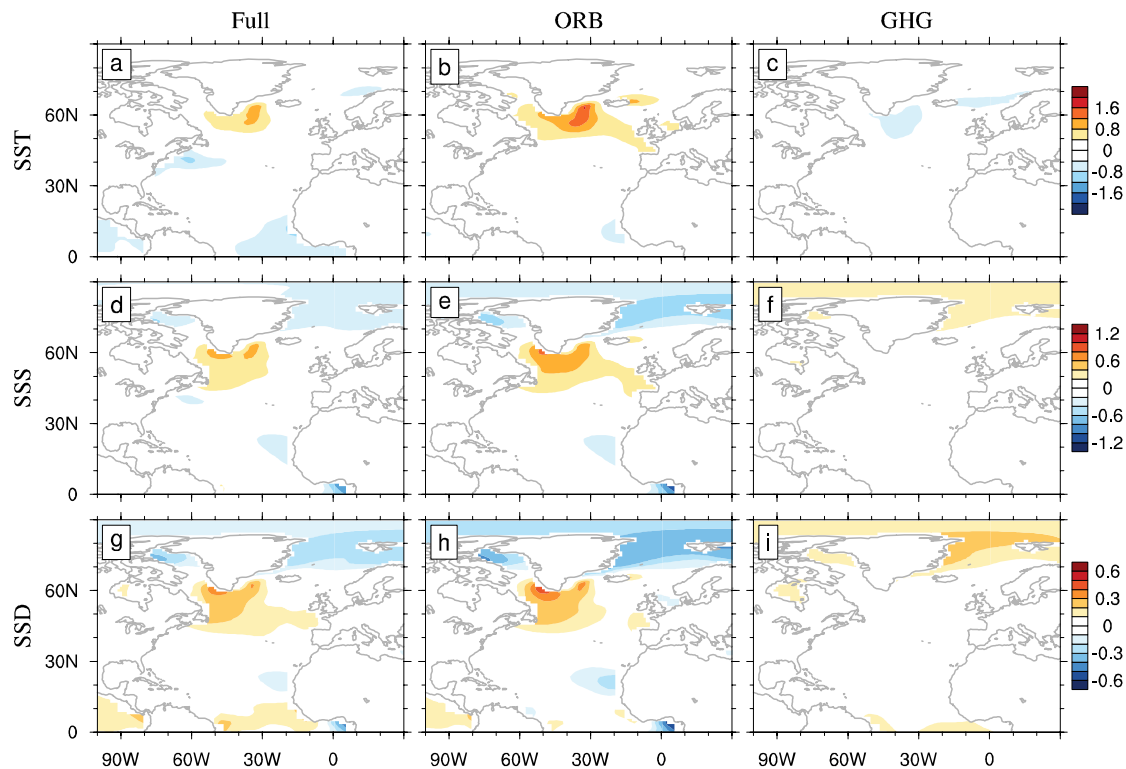


261

262 **Figure 8** Changes in (a)–(c) sea-surface temperature (SST), (d)–(f) sea-surface salinity (SSS), and (g)–(i) sea-surface density  
 263 (SSD) of the North Atlantic in Exp MH, with respect to Exp PI. (a), (d), and (g) are for the total changes; (b), (e), and (h),  
 264 for the changes due to ORB effect; (c), (f), and (i), for changes due to GHG effect. Units: °C for SST, psu for SSS, and kg/m<sup>3</sup>  
 265 for SSD.

266

267 The patterns of SSD difference (Figs. 8g–i) resemble those of both SSS and SST differences, while its polarity is  
 268 determined by SSS difference. The higher SSD in the North Atlantic is favorable for a stronger deep-water formation  
 269 and thus a stronger AMOC in Exp MH. Forced by the ORB effect, the North Atlantic surface ocean can be 0.5 kg/m<sup>3</sup>  
 270 denser in Exp MH than in Exp PI (Fig. 8h), which could have resulted in a 1.2-Sv stronger AMOC in Exp MH than in  
 271 Exp PI (Fig. 6e). However, the GHG effect, although weak, has an opposite effect on SSD and thus the AMOC (Fig.  
 272 8i), and eventually mitigates the ocean change in Exp MH. Similar patterns of SSD are shown in the transient  
 273 experiments, with increased North Atlantic density in Exp ORB, and the opposite and weaker effect in Exp GHG  
 274 (Figs. 9g, h, i), corresponding to changes in the AMOC (Fig. 6). These suggest that the mechanisms of ORB and GHG  
 275 on climate change in the equilibrium and transient experiments are consistent.



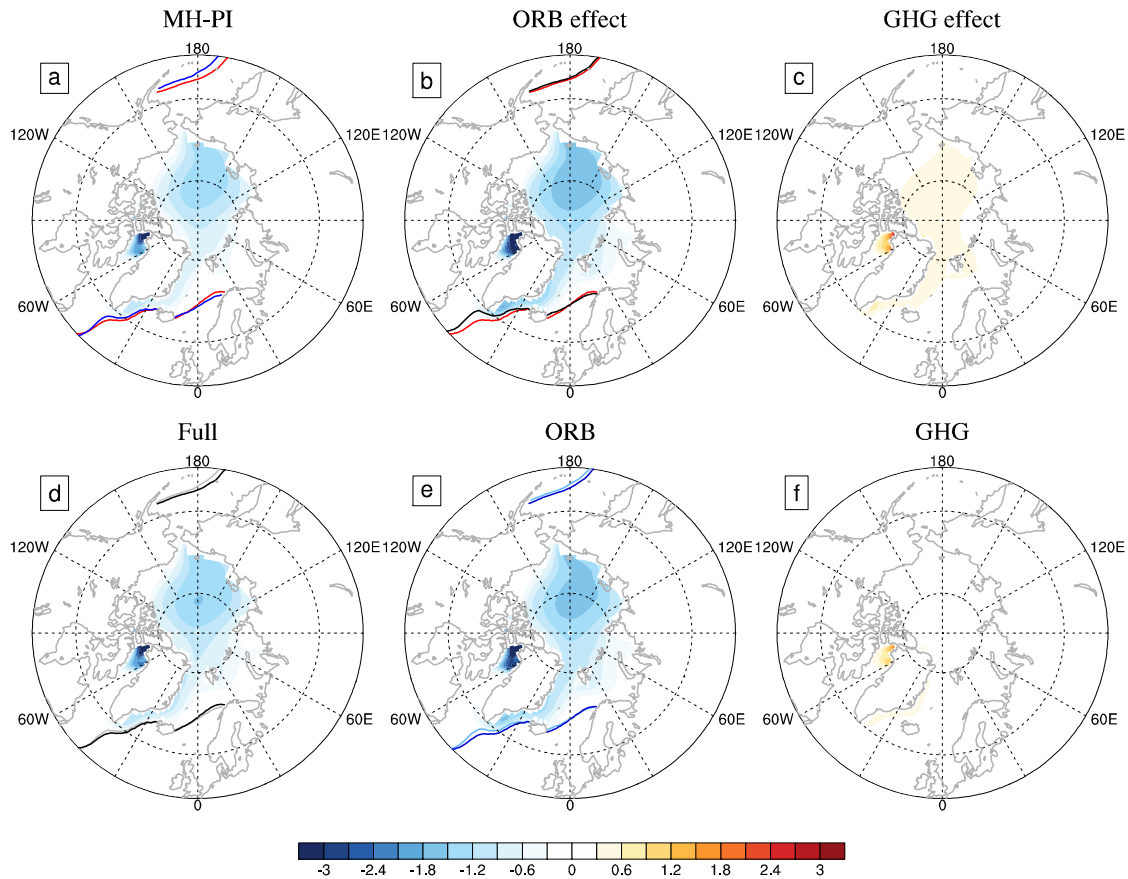
276

277 **Figure 9** Similar to Fig. 8, but for Exps Full, ORB, and GHG, respectively. All variables represents changes between the  
 278 **two stages (Stage1-Stage2).**

279

#### 280 **4.2 Change in surface freshwater flux**

281 Sea-surface freshwater flux includes both sea-ice formation (melting) and net evaporation (i.e., evaporation  
 282 minus precipitation, or EMP). Figure 10 shows the change of annual mean sea-ice thickness in the Arctic. The Arctic  
 283 sea-ice thickness in Exp MH is about 1.0 m thinner than that in Exp PI (Fig. 10a). The largest sea-ice difference,  
 284 which is about 3.0 m thinner in Exp MH, occurs in the Baffin Bay. When forced by the ORB effect only, the Arctic  
 285 sea ice would be more than 1.5 m thinner (Fig. 10b), consistent with the stronger insolation and the warming in the  
 286 NH high latitudes (Figs. 1, 2e). The GHG effect leads to a slight increase of sea ice in the Arctic (Fig. 10c) in Exp  
 287 MH, which is less than 0.5 m in thickness. Changes in Arctic sea-ice thickness can affect sea ice transport to the  
 288 subpolar Atlantic. The loss of sea ice in the central Arctic Ocean can reduce its export through the Fram Strait, which  
 289 can lead to an increase in salinity in the associated subpolar [no “-”] regions (Shi and Lohmann, 2016), as shown in  
 290 Figs. 8d and e. Similar changes in sea-ice thickness also occur in the transient experiments: the Arctic sea-ice  
 291 thickness is decreased significantly in Exp ORB, while it is nearly unchanged in Exp GHG (Figs. 10e, f), reflecting the  
 292 consistency of the effects of ORB and GHG in both equilibrium and transient experiments.

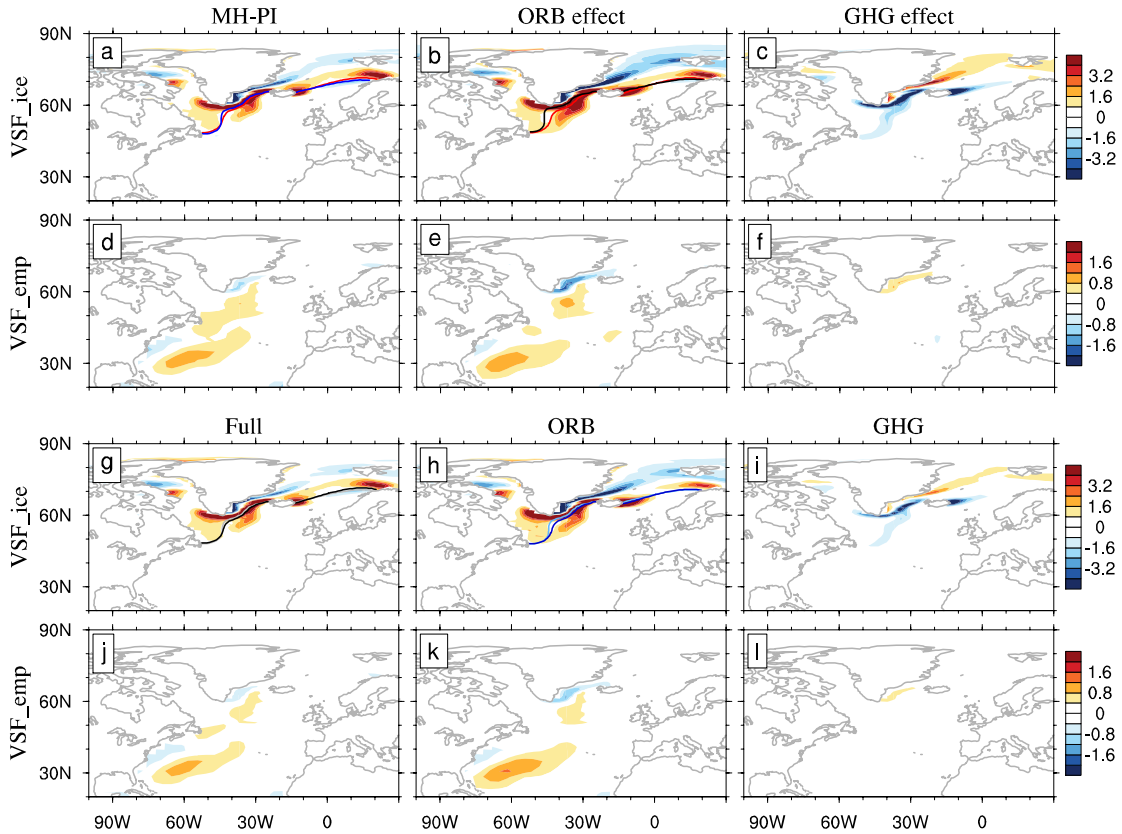


293

294 **Figure 10** (a)–(c) Changes in Arctic mean sea-ice thickness in Exp MH, with respect to Exp PI. Positive (negative) value  
 295 represents sea-ice formation (melting). (a) is for the total change; (b) and (c), for changes due to ORB and GHG effects,  
 296 respectively. Solid blue, black, and red curves show the sea-ice margin in Exps MH, MH\_ORB and PI, respectively. (d)–(f)  
 297 Same as (a)–(c), except for Exps Full, ORB, and GHG, respectively. The solid gray and light blue curves indicate the sea-ice  
 298 margin of Stage1 in Exps Full and ORB, respectively; and the black and dark blue solid curves represent the sea-ice margin  
 299 of Stage2 in Exps Full and ORB, respectively. The sea-ice margin is defined by the 15% sea-ice fraction. Units: m.

300

301 The sea-ice margin in the North Atlantic in Exp MH is slightly more northward compared to that in Exp PI (solid  
 302 blue curve, Fig. 11a). The curves in Fig. 11 show sea-ice margin in different experiments. The northward displacement  
 303 of sea-ice margin and the decrease in sea-ice volume in the Arctic favor the decrease in freshwater flux in the North  
 304 Atlantic, helping a more saline North Atlantic, which contributes about  $0.9 \text{ psu } 10\text{yr}^{-1}$  to the SSS tendency between  
 305  $40^\circ$  and  $60^\circ\text{N}$  (Fig. 11a). The EMP flux is small, and the upper ocean is refreshed at a steady rate of about  $0.09 \text{ psu } 10$   
 306  $\text{yr}^{-1}$  in the North Atlantic (Fig. 11d). The contributions of sea-ice change and EMP flux to SSS in the transient  
 307 experiments are also about  $0.9$  and  $0.09 \text{ psu } 10 \text{ yr}^{-1}$ , respectively (Figs. 11g, j). Overall, for the North Atlantic the  
 308 change of sea ice plays a dominant role; and its contribution to SSS tendency is about 10 times that of EMP.



309

310 **Figure 11** Changes in (a)–(c), namely, virtual salt flux (VSF) due to sea ice, and in (d)–(f), VSF due to EMP in Exp MH,  
 311 with respect to Exp PI. Positive (negative) value represents sea-ice formation (melting) or evaporation larger (smaller) than  
 312 precipitation. (a) and (d) are for total changes; (b) and (e), for changes due to ORB effect; (c) and (f), for GHG effect. (g)–(l)  
 313 Same as (a)–(f), but for Exp Full, Exp ORB, and Exp GHG, respectively. The solid gray and light blue curves indicate the  
 314 sea-ice margin of Stage1 in Exps Full and ORB, respectively; and the black and dark blue solid curves represent the sea-ice  
 315 margin of Stage2 in Exps Full and ORB, respectively. The sea-ice margin in (a)–(b) is defined the same way as that in Fig. 8.  
 316 Units:  $\text{psu } 10 \text{ yr}^{-1}$ .

317

318 The sea-ice margin in Exp MH is controlled by the ORB effect. In individual forcing experiment, the sea-ice  
 319 margin forced by the ORB effect is almost the same as that in Exp MH (solid black curve, Fig. 11b). The contributions  
 320 of ORB and GHG effects to changes in virtual salt flux (VSF) due to sea ice are 1.3 and  $-0.4 \text{ psu } 10 \text{ yr}^{-1}$ , respectively  
 321 (Figs. 11b, c); and those due to the EMP flux are 0.06 and  $0.03 \text{ psu } 10 \text{ yr}^{-1}$ , respectively (Figs. 11e, f). In the transient  
 322 experiments, the contributions of ORB and GHG effects to the VSF due to sea ice are 1.1 and  $-0.2 \text{ psu } 10 \text{ yr}^{-1}$ ,  
 323 respectively (Figs. 11h, i); and those due to EMP flux are 0.05 and  $0.03 \text{ psu } 10 \text{ yr}^{-1}$ , respectively (Figs. 11i, l). This  
 324 suggests that the sea-ice change caused by the ORB effect plays an important role in the enhancement of the AMOC in  
 325 Exp MH.



326 In general, the modelling results suggest that the stronger AMOC in the MH period resulted from more saline  
327 North Atlantic, which was contributed mainly by smaller freshwater flux coming from the Arctic. The contribution of  
328 EMP to salinity change was small, which was only one-tenth of the sea-ice contribution. ORB and GHG consistently  
329 play opposite roles in the deep-water formation of the subpolar Atlantic. Their combined effect resulted in little  
330 change in the AMOC in the MH period, which is less than 1 Sv enhancement in both equilibrium and transient  
331 experiments.

332

## 333 **5. Summary and discussion**

334 In this study, six experiments using the CESM1.0 were conducted to quantify the contributions of ORB and GHG  
335 effects to the MH climate. Most attention was paid to the AMOC; and the mechanism to the insignificant difference of  
336 the AMOC between the MH and PI periods was explored. This study is the first attempt to separate the ORB and GHG  
337 effects on the MH climate. Simulations showed that the NH climate exhibits much greater regional and seasonal  
338 variability due to the seasonal enhancement of insolation caused by changes in ORB; and these contrasting seasonal  
339 responses lead to little change in annual mean climate. Lower GHG in Exp MH has a global cooling effect, with  
340 greater temperature decreases at higher latitudes associated with feedbacks from sea ice and snow cover. The  
341 combined effect of these two forcing factors leads to a weak warming at the NH high latitudes and cooling elsewhere,  
342 similar to the temperature changes in the PMIP4 ensemble (Brierley et al., 2020).

343 Weakening meridional atmospheric temperature gradient in Exp MH leads to the Hadley cell being weakened by  
344 about 10% in the NH. At the same time, due to the change of sea-surface buoyancy in the North Atlantic, the AMOC  
345 is slightly enhanced by about 4%. As far as the changes in MHT magnitude in the NH are concerned, the effect of  
346 ORB is about five times that of GHG. Our experiments also showed that the change in the AMOC is mostly  
347 determined by the freshwater flux change in the North Atlantic, which is in turn closely related to the Arctic sea-ice  
348 change related to the ORB effect. GHG has the opposite effect to ORB, which mitigates the enhancement of the  
349 AMOC (Figs. 9b, c).

350 The conclusions drawn in this paper may be model-dependent. Shi and Lohmann (2016) simulated a stronger MH  
351 AMOC in the high-resolution version of the ECHAM, with a maximum change of more than 2 Sv. Most of the models  
352 in the CMIP5 reveal a positive AMOC change in the MH period. Some previous studies (Ganopolski et al., 1998;  
353 Otto-Bliesner et al., 2006) showed that the AMOC in the MH is weaker than that of the PI period. The main reason for  
354 the inconsistency is that the simulated ocean salinity in the North Atlantic is different. Therefore, it is necessary to

355 carry out simulations with multiple models to reduce model dependence. Our simulations of the AMOC in the MH are  
356 similar to those of Jiang et al. (2023), both showing no significant changes in the AMOC in the MH compared with  
357 the PI; however, their study did not explain the mechanism behind this phenomenon. Our study reveals the  
358 competitive relationship between the two forcing factors through multiple-equilibrium state simulations and transient  
359 simulations, supporting the popular conclusions about the AMOC change from the MH to the PI periods.

360 Our study focuses on the effects of ORB and GHG; and the simulated cooler annual mean temperature in most  
361 areas of the NH differs from the warming record revealed by most proxy data (Wanner et al., 2008; Liu et al., 2014),  
362 but is similar to the conclusions from the PMIP4 simulations. It is unclear whether these differences originate from the  
363 model, the data record, or a combination of the two. Some proxy data suggested that the climate of North Africa was  
364 wetter in the MH period, which was known as the Green Sahara (Larrosaana, 2012). Jiang et al. (2012) analyzed the  
365 simulation results of six coupled models in PMIP2 for the MH period. They found that the dynamic vegetation effect  
366 led to a decrease in annual cooling over China in five of these models during the MH period, although its impact on  
367 the MH temperature was minimal. Braconnot et al. (2021) and Zhang et al. (2021a) studied the effect of dust reduction  
368 on climate due to the greening of the Sahara desert, using the CESM and IPSL models, respectively, showing global  
369 mean surface temperature increased by about 0.1°C. Although there are other forcing factors in the MH period, such  
370 as vegetation, dust, and topography, overall our simulations are representative of the most important forcing factors  
371 and provide quantified estimates of the contributions of ORB and GHG effects on the MH climate.

372

373 **Acknowledgements.** This work is supported by the National Natural Science Foundation of China (Nos. 42230403,  
374 42288101, and 41725021) and by the foundation at the Shanghai Frontiers Science Centre of Atmosphere-Ocean  
375 Interaction of Fudan University. The experiments were performed on the supercomputers at the Chinese National  
376 Supercomputer Centre in Tianjin (Tian-He No.1).

377

378 **References**

- 379 Berger, A. and Loutre, M. F.: Insolation values for the climate of the last 10 million years, *Quaternary Sci. Rev.*, 10,  
380 297-317, [https://doi.org/10.1016/0277-3791\(91\)90033-Q](https://doi.org/10.1016/0277-3791(91)90033-Q), 1991.
- 381 Braconnot, P., Albani, S., Balkanski, Y., Cozic, A., Kageyama, M., Sima, A., Marti, O., and Peterschmitt, J. Y.:  
382 Impact of dust in PMIP-CMIP6 mid-Holocene simulations with the IPSL model, *Clim. Past*, 17, 1091-1117,  
383 <http://doi.org/10.5194/cp-17-1091-2021>, 2021.
- 384 Brierley, C. M., Zhao, A., Harrison, S. P., Braconnot, P., Williams, C. J. R., Thornalley, D. J. R., Shi, X., Peterschmitt,  
385 J.-Y., Ohgaito, R., Kaufman, D. S., Kageyama, M., Hargreaves, J. C., Erb, M. P., Emile-Geay, J., D'Agostino, R.,  
386 Chandan, D., Carré, M., Bartlein, P. J., Zheng, W., Zhang, Z., Zhang, Q., Yang, H., Volodin, E. M., Tomas, R.  
387 A., Routson, C., Peltier, W. R., Otto-Bliesner, B., Morozova, P. A., McKay, N. P., Lohmann, G., Legrande, A.  
388 N., Guo, C., Cao, J., Brady, E., Annan, J. D., and Abe-Ouchi, A.: Large-scale features and evaluation of the  
389 PMIP4-CMIP6 <i>midHolocene</i> simulations, *Clim. Past*, 16, 1847-1872,  
390 <https://doi.org/10.5194/cp-16-1847-2020>, 2020.
- 391 Brown, N. and Galbraith, E. D.: Hosed vs. unhosed: interruptions of the Atlantic Meridional Overturning Circulation  
392 in a global coupled model, with and without freshwater forcing, *Clim. Past*, 12, 1663-1679,  
393 <https://doi.org/10.5194/cp-12-1663-2016>, 2016.
- 394 Chen, C.-T. A., Lan, H.-C., Lou, J.-Y., and Chen, Y.-C.: The Dry Holocene Megathermal in Inner Mongolia,  
395 *Palaeogeogr. Palaeoclimatol. Palaeoecol.*, 193, 181-200, [https://doi.org/10.1016/s0031-0182\(03\)00225-6](https://doi.org/10.1016/s0031-0182(03)00225-6), 2003.
- 396 Czaja, A. and Marshall, J.: The Partitioning of Poleward Heat Transport between the Atmosphere and Ocean, *Global*  
397 *Planet. Change.*, 63, 1498-1511, <https://doi.org/10.1175/jas3695.1>, 2006.
- 398 Fox-Kemper, B., H.T. Hewitt, C. Xiao, G. Aðalgeirsdóttir, S.S. Drijfhout, T.L. Edwards, N.R. Golledge, M. Hemer,  
399 R.E. Kopp, G. Krinner, A. Mix, D. Notz, S. Nowicki, I.S. Nurhati, L. Ruiz, J.-B. Sallée, A.B.A. Slangen, and Y.  
400 Yu: Ocean, cryosphere and sea level change. In V. Masson-Delmotte, P. Zhai, A. Pirani, S. L. Connors, C. Péan,  
401 S. Berger, et al. (Eds.), *Climate change 2021: The physical science basis. Contribution of working group I to the*  
402 *sixth assessment report of the intergovernmental panel on climate change (chap. 9)*. Cambridge University Press,  
403 <https://doi.org/10.1017/9781009157896.011>, 2021.
- 404 Găinușă-Bogdan, A., Swingedouw, D., Yiou, P., Cattiaux, J., Codron, F., and Michel, S.: AMOC and summer sea ice  
405 as key drivers of the spread in mid-holocene winter temperature patterns over Europe in PMIP3 models, *Global*  
406 *Planet. Change.*, 184, <https://doi.org/10.1016/j.gloplacha.2019.103055>, 2020.

407 Ganopolski, A., Kubatzki, C., Claussen, M., Brovkin, V., and Petoukhov, V.: The Influence of Vegetation-  
408 Atmosphere-Ocean Interaction on Climate During the Mid-Holocene, *Science*, 280, 1916-1919,  
409 <https://doi.org/10.1126/science.280.5371.1916>, 1998.

410 Held, I. M.: The Partitioning of the Poleward Energy Transport between the Tropical Ocean and Atmosphere, *J.*  
411 *Atmos. Sci.*, 58, 943-948, [https://doi.org/10.1175/1520-0469\(2001\)058<0943:Tpotpe>2.0.Co;2](https://doi.org/10.1175/1520-0469(2001)058<0943:Tpotpe>2.0.Co;2), 2001.

412 Hunke, E. C. and Lipscomb, W. H.: CICE: The Los Alamos Sea Ice Model documentation and software user's  
413 manual, version 4.1. Doc. LACC-06-012, 76, [CICE documentation and software user's manual.pdf](#)  
414 [colorado.edu](http://colorado.edu), 2010.

415 Jiang, D., Lang, X., Tian, Z., and Wang, T.: Considerable Model–Data Mismatch in Temperature over China during  
416 the Mid-Holocene: Results of PMIP Simulations, *J. Climate*, 25, 4135-4153, [https://doi.org/10.1175/jcli-d-11-](https://doi.org/10.1175/jcli-d-11-00231.1)  
417 [00231.1](https://doi.org/10.1175/jcli-d-11-00231.1), 2012.

418 Jiang, Z., Brierley, C., Thornalley, D., and Sax, S.: No changes in overall AMOC strength in interglacial PMIP4 time  
419 slices, *Clim. Past*, 19, 107-121, <https://doi.org/10.5194/cp-19-107-2023>, 2023a.

420 Jiang, Z., Brierley, C. M., Bader, J., Braconnot, P., Erb, M., Hopcroft, P. O., Jiang, D., Jungclaus, J., Khon, V.,  
421 Lohmann, G., Marti, O., Osman, M. B., Otto-Bliesner, B., Schneider, B., Shi, X., Thornalley, D. J. R., Tian, Z.,  
422 and Zhang, Q.: No Consistent Simulated Trends in the Atlantic Meridional Overturning Circulation for the Past  
423 6,000 Years, *Geophysical Research Letters*, 50, e2023GL103078, <https://doi.org/10.1029/2023GL103078>, 2023b.

424 Jin, G.: Mid-Holocene climate change in North China, and the effect on cultural development, *Chinese Sci. Bull.*, 47,  
425 <https://doi.org/10.1360/02tb9095>, 2002.

426 Joussaume, S. and Taylor, K.: Status of the paleoclimate modeling intercomparison project (PMIP), *World*  
427 *Meteorological Organization-Publications-WMO TD*, 425-430, 1995.

428 Kageyama, M., Braconnot, P., Harrison, S. P., Haywood, A. M., Jungclaus, J. H., Otto-Bliesner, B. L., Peterschmitt,  
429 J.-Y., Abe-Ouchi, A., Albani, S., Bartlein, P. J., Brierley, C., Crucifix, M., Dolan, A., Fernandez-Donado, L.,  
430 Fischer, H., Hopcroft, P. O., Ivanovic, R. F., Lambert, F., Lunt, D. J., Mahowald, N. M., Peltier, W. R., Phipps, S.  
431 J., Roche, D. M., Schmidt, G. A., Tarasov, L., Valdes, P. J., Zhang, Q., and Zhou, T.: The PMIP4 contribution to  
432 CMIP6 – Part 1: Overview and over-arching analysis plan, *Geosci. Model. Dev.*, 11, 1033-1057,  
433 <https://doi.org/10.5194/gmd-11-1033-2018>, 2018.

434 Larrasoana, J.: A Northeast Saharan Perspective on Environmental Variability in North Africa and its Implications for  
435 Modern Human Origins, *Modern Origins: A North African Perspective*, 19-34, 10.1007/978-94-007-2929-2\_2,  
436 2012.

437 Lawrence, D. M., Oleson, K. W., Flanner, M. G., Fletcher, C. G., Lawrence, P. J., Levis, S., Swenson, S. C., and  
438 Bonan, G. B.: The CCSM4 Land Simulation, 1850–2005: Assessment of Surface Climate and New Capabilities,  
439 J. Climate, 25, 2240-2260, <https://doi.org/10.1175/jcli-d-11-00103.1>, 2012.

440 Liu, Z., Zhu, J., Rosenthal, Y., Zhang, X., Otto-Bliesner, B. L., Timmermann, A., Smith, R. S., Lohmann, G., Zheng,  
441 W., and Elison Timm, O.: The Holocene temperature conundrum, P. Natl. Acad. Sci. USA, 111, E3501-3505,  
442 <https://doi.org/10.1073/pnas.1407229111>, 2014.

443 Monnin, E., Indermuhle, A., Dillenbach, A., Fluckiger, J., Stauffer, B., Stocker, T. F., Raynaud, D., and Barnola,  
444 J.-M.: Atmospheric CO<sub>2</sub> Concentrations over the Last Glacial Termination, Science, 291, 112-114,  
445 <https://doi.org/10.1126/science.291.5501.112>, 2001.

446 Monnin, E., Steig, E. J., Siegenthaler, U., Kawamura, K., Schwander, J., Stauffer, B., Stocker, T. F., Morse, D. L.,  
447 Barnola, J.-M., Bellier, B., Raynaud, D., and Fischer, H.: Evidence for substantial accumulation rate variability in  
448 Antarctica during the Holocene, through synchronization of CO<sub>2</sub> in the Taylor Dome, Dome C and DML ice  
449 cores, Earth Planet. Sc. Lett., 224, 45-54, <https://doi.org/10.1016/j.epsl.2004.05.007>, 2004.

450 Moss, M. L., Peteet, D. M., and Whitlock, C.: Mid-Holocene culture and climate on the Northwest Coast of North  
451 America, in: Climate Change and Cultural Dynamics, 491-529, [https://doi.org/10.1016/b978-012088390-](https://doi.org/10.1016/b978-012088390-5.50019-4)  
452 [5.50019-4](https://doi.org/10.1016/b978-012088390-5.50019-4), 2007.

453 Otto-Bliesner, B. L., Brady, E. C., Clauzet, G., Tomas, R., Levis, S., and Kothavala, Z.: Last Glacial Maximum and  
454 Holocene Climate in CCSM3, J. Climate, 19, 2526-2544, <https://doi.org/10.1175/jcli3748.1>, 2006.

455 Otto-Bliesner, B. L., Braconnot, P., Harrison, S. P., Lunt, D. J., Abe-Ouchi, A., Albani, S., Bartlein, P. J., Capron, E.,  
456 Carlson, A. E., Dutton, A., Fischer, H., Goelzer, H., Govin, A., Haywood, A., Joos, F., LeGrande, A. N.,  
457 Lipscomb, W. H., Lohmann, G., Mahowald, N., Nehrbass-Ahles, C., Pausata, F. S. R., Peterschmitt, J.-Y.,  
458 Phipps, S. J., Renssen, H., and Zhang, Q.: The PMIP4 contribution to CMIP6 – Part 2: Two interglacials,  
459 scientific objective and experimental design for Holocene and Last Interglacial simulations, Geosci. Model. Dev.,  
460 10, 3979-4003, <https://doi.org/10.5194/gmd-10-3979-2017>, 2017.

461 Park, S., Bretherton, C. S., and Rasch, P. J.: Integrating Cloud Processes in the Community Atmosphere Model,  
462 Version 5, J. Climate, 27, 6821-6856, <https://doi.org/10.1175/jcli-d-14-00087.1>, 2014.

463 Rahmstorf, S.: Thermohaline Ocean Circulation, in: Encyclopedia of Quaternary Sciences, edited by: Elias, S. A.,  
464 Elsevier, Amsterdam, 1–10, 2006.

465 Roberts, N., Eastwood, W. J., Kuzucuoğlu, C., Fiorentino, G., and Caracuta, V.: Climatic, vegetation and cultural  
466 change in the eastern Mediterranean during the mid-Holocene environmental transition, *The Holocene*, 21, 147-  
467 162, <https://doi.org/10.1177/0959683610386819>, 2011.

468 Rossignol-Strick, M.: The Holocene climatic optimum and pollen records of sapropel 1 in the eastern Mediterranean,  
469 9000–6000BP, *Quaternary Sci. Rev.*, 18, 515-530, [https://doi.org/10.1016/S0277-3791\(98\)00093-6](https://doi.org/10.1016/S0277-3791(98)00093-6), 1999.

470 Sandweiss, D. H., Maasch, K. A., and Anderson, D. G.: Transitions in the Mid-Holocene, *Science*, 283, 499-500,  
471 <https://doi.org/10.1126/science.283.5401.499>, 1999.

472 Shi, X. and Lohmann, G.: Simulated response of the mid-Holocene Atlantic meridional overturning circulation in  
473 ECHAM6-FESOM/MPIOM, *J. Geophys. Res.-Oceans*, 121, 6444-6469, <https://doi.org/10.1002/2015jc011584>,  
474 2016.

475 Shi, X., Werner, M., Wang, Q., Yang, H., and Lohmann, G.: Simulated Mid-Holocene and Last Interglacial Climate  
476 Using Two Generations of AWI-ESM, *J. Climate*, 35, 4211-4231, <https://doi.org/10.1175/jcli-d-22-0354.1>, 2022.

477 Smith, R. and Gent, P.: The Parallel Ocean Program (POP) reference manual, Los Alamos Unclassified Report LA-  
478 UR-02-2484, 2010.

479 Trenberth, K. E. and Caron, J. M.: Estimates of Meridional Atmosphere and Ocean Heat Transports, *J. Climate*, 14,  
480 3433-3443, [https://doi.org/10.1175/1520-0442\(2001\)014<3433:Eomaa>2.0.Co;2](https://doi.org/10.1175/1520-0442(2001)014<3433:Eomaa>2.0.Co;2), 2001.

481 Wanner, H., Beer, J., Bütikofer, J., Crowley, T. J., Cubasch, U., Flückiger, J., Goosse, H., Grosjean, M., Joos, F.,  
482 Kaplan, J. O., Küttel, M., Müller, S. A., Prentice, I. C., Solomina, O., Stocker, T. F., Tarasov, P., Wagner, M.,  
483 and Widmann, M.: Mid- to Late Holocene climate change: an overview, *Quaternary Sci. Rev.*, 27, 1791-1828,  
484 <https://doi.org/10.1016/j.quascirev.2008.06.013>, 2008.

485 Warden, L., Moros, M., Neumann, T., Shennan, S., Timpson, A., Manning, K., Sollai, M., Wacker, L., Perner, K.,  
486 Häusler, K., Leipe, T., Zillén, L., Kotilainen, A., Jansen, E., Schneider, R. R., Oeberst, R., Arz, H., and Sinninghe  
487 Damsté, J. S.: Climate induced human demographic and cultural change in northern Europe during the mid-  
488 Holocene, *Sci. Rep-UK*, 7, <https://doi.org/10.1038/s41598-017-14353-5>, 2017.

489 Williams, C. J. R., Guarino, M.-V., Capron, E., Malmierca-Vallet, I., Singarayer, J. S., Sime, L. C., Lunt, D. J., and  
490 Valdes, P. J.: CMIP6/PMIP4 simulations of the mid-Holocene and Last Interglacial using HadGEM3:  
491 comparison to the pre-industrial era, previous model versions and proxy data, *Clim. Past*, 16, 1429-1450,  
492 <https://doi.org/10.5194/cp-16-1429-2020>, 2020.

493 Wunsch, C.: The Total Meridional Heat Flux and Its Oceanic and Atmospheric Partition, *J. Climate*, 18, 4374-4380,  
494 <https://doi.org/10.1175/jcli3539.1>, 2005.

495 Yan, M. and Liu, J.: Physical processes of cooling and mega-drought during the 4.2 ka BP event: results from  
496 TraCE-21ka simulations, *Clim. Past*, 15, 265-277, <https://doi.org/10.5194/cp-15-265-2019>, 2019.

497 Zhang, J., Kong, X., Zhao, K., Wang, Y., Liu, S., Wang, Z., Liu, J., Cheng, H., and Edwards, R. L.: Centennial-scale  
498 climatic changes in Central China during the Holocene climatic optimum, *Palaeogeogr. Palaeoclimatol.*  
499 *Palaeoecol.*, 558, <https://doi.org/10.1016/j.palaeo.2020.109950>, 2020.

500 Zhang, M., Liu, Y., Zhang, J., and Wen, Q.: AMOC and Climate Responses to Dust Reduction and Greening of  
501 Sahara during the Mid-Holocene, *J. Climate*, 1-59, <https://doi.org/10.1175/jcli-d-20-0628.1>, 2021a.

502 Zhang, Q., Berntell, E., Axelsson, J., Chen, J., Han, Z., de Nooijer, W., Lu, Z., Li, Q., Zhang, Q., Wyser, K., and  
503 Yang, S.: Simulating the mid-Holocene, last interglacial and mid-Pliocene climate with EC-Earth3-LR, *Geosci.*  
504 *Model. Dev.*, 14, 1147-1169, <https://doi.org/10.5194/gmd-14-1147-2021>, 2021b.

505